



A first-principles study of oxygen vacancy induced changes in structural, electronic and magnetic properties of $\text{La}_{2/3}\text{Sr}_{1/3}\text{MnO}_3$



Jia Li ^a, Lizhong Sun ^{a,b}, Prathamesh M. Shenai ^a, Junling Wang ^a, Hang Zheng ^c, Yang Zhao ^{a,*}

^a Division of Materials Science, Nanyang Technological University, Singapore, 639798, Singapore

^b Laboratory for Quantum Engineering and Micro-Nano Energy Technology, Xiangtan University, Xiangtan, Hunan, 411105, China

^c Department of Physics, Shanghai Jiao Tong University, 800 Dong Chuan Road, Shanghai, 200240, China

ARTICLE INFO

Article history:

Received 2 November 2014

Received in revised form

9 June 2015

Accepted 13 July 2015

Available online 17 July 2015

Keywords:

LaSrMnO_3

Perovskite manganese oxides

DFT calculations

Oxygen vacancies

ABSTRACT

We have systematically assessed the influence of oxygen vacancy defects on the structural, electronic and magnetic properties of $\text{La}_{2/3}\text{Sr}_{1/3}\text{MnO}_3$ via first-principles calculations using the bare GGA as well as the GGA + U formalism. The on-site Coulombic repulsion parameter U for Mn 3d orbital in the latter has been determined by the linear response theory. It is revealed that the introduction of the vacancy defects causes prominent structural changes in the microenvironment of a defect including the distortions of MnO_6 octahedra. In contrast to the general notion, the GGA + U formalism is found to yield significantly more prominent structural changes than the bare GGA method. The octahedral distortion leads to a strengthening or weakening of the hybridization between Mn 3d and O 2p orbitals depending upon an increase or decrease, respectively, in the Mn–O distances as compared to the pristine system. The magnetic moments of the Mn atoms located in three typical sites of the vacancy-containing supercell are all larger than those in the pristine system. This enhancement for the Mn atoms located in the first- and third-nearest neighboring MnO_6 octahedra of the vacancy defect originates from the electron transfer from 4s/3p to 3d orbitals. On the other hand, for the Mn atom located in the first-nearest neighboring site of the vacancy it is attributed to the increased total number of electrons in 3d orbitals due to the absence of one Mn–O bond. Furthermore, we have characterized the O-vacancy defect as a hole-type defect that forms a negative charge center, attracting electrons.

© 2015 Elsevier B.V. All rights reserved.

1. Introduction

The perovskite manganese oxides $\text{La}_{1-x}\text{A}_x\text{MnO}_3$ (A = Ca, Ba, Sr) have attracted extensive research attention thanks to their special electronic and magnetic properties as well as their potential applications [1–3]. Among this group of the materials, $\text{La}_{1-x}\text{Sr}_x\text{MnO}_3$ (LSMO) exhibits exotic properties such as colossal magnetoresistance (CMR) and metal-insulator transition [4], which originate from a delicate coupling between charge, spin, orbital and lattice degrees of freedom. Heterostructures based on LSMO also possess exciting physical properties such as a large magnetoresistivity in LSMO sandwiched by carbon nanotubes [5], magnetoelectric effects in LSMO/piezoelectric and LSMO/ferroelectric interfaces [6], and proximity effects in ferromagnetic/superconducting

heterostructures [7]. The optimally doped $\text{La}_{0.66}\text{A}_{0.33}\text{MnO}_3$ exhibits half-metallic behavior and ferromagnetism, rendering it one of the most technologically attractive classes of materials in the context of spin injection, given the high Curie temperature and large spin polarization at the Fermi level reaching nearly 100% below the Curie ordering temperature. For example, $\text{La}_{0.66}\text{A}_{0.33}\text{MnO}_3$ based LSMO/SrTiO₃/LSMO magnetic tunneling junctions were found to exhibit a tunnel magnetoresistance ratio larger than 1800% [8].

Oxygen vacancy defects are believed to play an important role in giving rise to the unique properties of perovskite manganese oxides. In an important work, a two-dimensional electron gas has been found at the interface between SrTiO₃ and LaAlO₃ and the origin of the charge in heterostructures comprised of these two materials is attributed to the oxygen vacancies [9,10]. It is also found recently that oxygen vacancy defects can be rather easily formed on the (001) surface of NdAlO₃, resulting in surface reconstruction and the formation of a zigzag -Al–O–Al- chain,

* Corresponding author.

E-mail address: YZhao@ntu.edu.sg (Y. Zhao).

which quenches the built-in potential and significantly enhances the carrier density [11]. Picozzi et al. reported that the oxygen vacancies cause prominent changes in the electronic and magnetic structures of $\text{La}_{0.66}\text{Sr}_{0.33}\text{MnO}_3$ [12]. While it was found that the valence band features shift toward higher binding energies and the degree of covalency of Mn bonding increases, it should be noted that their results focusing on the unrelaxed structure do not take into account the tilting of MnO_6 octahedra. From the crystallographic perspective, the MnO_6 octahedra are important features of the perovskite manganese oxides, and the existence of an oxygen vacancy in an octahedron may lead to a change in its structure via correlated deformation and rotation of neighboring octahedra. Such vacancy induced structural changes in MnO_6 octahedra may play an important role in influencing the electronic and magnetic properties, yet, have not been studied previously to the best of our knowledge. As a result, there exists a pressing need to address the issue of the influence of oxygen vacancies on the properties of LSMO.

In this study, we have carried out the density functional theory (DFT) -based first-principles calculations by using the generalized gradient approximation (GGA) formalism as well as its modified form GGA + U to investigate the oxygen vacancy induced changes in the structural, electronic and magnetic properties of $\text{La}_{2/3}\text{Sr}_{1/3}\text{MnO}_3$. In addition, the formation energy of an oxygen vacancy with different charge states is calculated, leading to assessment of their stability as well. The rest of the paper is organized as follows. Section 2 presents computational and theoretical details. In Section 3, results obtained on structural, electronic and magnetic properties of oxygen vacancy-containing LSMO systems as well as a comparison with the pristine system are presented and discussed in detail. Conclusions are drawn in the final Section 4.

2. Computational and theoretical details

To investigate the properties of LSMO, we employ a perovskite unit cell $\text{La}_{2/3}\text{Sr}_{1/3}\text{MnO}_3$ with lattice parameters $a = b = c = 3.876 \text{ \AA}$ [13,14]. In order to avoid interactions between the defects, we choose a sufficiently large $3 \times 3 \times 4$ supercell, which contains 180 atoms. The choice of 4 unit cells along the c axis is dictated by the requirement of setting the antiferromagnetic ordering. An oxygen vacancy is introduced by removing the O atom located at the center of the supercell. In our simulations, therefore, the concentration of oxygen vacancies is about 0.9%. We consider three supercells with

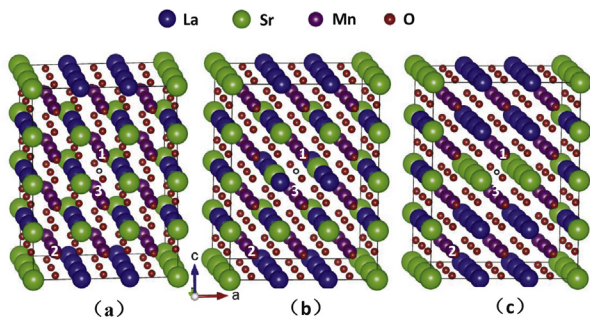


Fig. 1. Three configurations of $3 \times 3 \times 4$ supercell for $\text{La}_{0.66}\text{Sr}_{0.33}\text{MnO}_3$ containing one oxygen vacancy at the center denoted by a hollow circle. The number of Sr atoms (green spheres) as first-nearest neighbors of the vacancy in the ab -plane is (a) zero (b) two and (c) three. The blue, pink and red spheres correspond to La, Mn and O atoms, respectively. Mn Atoms labeled as 1 (Mn_1) and 2 (Mn_2) reside in the first-nearest neighboring and the third-nearest neighboring MnO_6 octahedron of the vacancy, respectively, while 3 (Mn_3) is a first-nearest neighbor of the vacancy. (For interpretation of the references to colour in this figure legend, the reader is referred to the web version of this article.)

different Sr substitutional sites as shown in Fig. 1. The number of Sr atoms located at the first nearest neighbor sites of the vacancy defect in the ab -plane is zero in Fig. 1(a), two in Fig. 1(b) and four in Fig. 1(c). The most energetically favorable configuration is then determined via the calculation of the total energy, and used for all the subsequent calculations. In addition, we calculate the total energy of LSMO in three different magnetic ordering states, i.e. A-type antiferromagnetic, G-type antiferromagnetic and ferromagnetic ordering, to determine the most stable configuration. The initial structure is then subjected to geometry optimization during which the lattice parameters and symmetry of supercell are constrained, and atomic positions are relaxed until the forces are quenched to the desired convergence criterion.

It is well known that first-principles calculations based on DFT for the strongly correlated systems such as LSMO, need to adopt formalisms going beyond the bare local density approximation (LDA) or GGA formalisms. Such formalisms include GGA (LDA) + U (U is the on-site Coulombic repulsion potential), GW and hybrid functionals, which yield band gaps in a better agreement with the experimental values [15,16]. The GGA + U approach is useful in treating systems containing transition metals in a much more computationally efficient manner than the GW and hybrid functionals approaches. Our first-principles calculations are carried out by using both the standard GGA and the GGA + U energy functional, in the latter of which, the value of U for Mn d electrons is calculated with the linear response theory. All the calculations in this work are carried out with the Vienna ab initio simulation package (VASP) [17,18]. The core–electron interactions are modeled by the projector-augmented wave potentials [19] and the Perdew–Burke–Ernzerhof-correlation functional is adopted [20,21]. We have adopted the valence electrons configuration as $5s^2 5p^6 5d^1 6s^2$ for La, $3s^2 3p^6 4s^2$ for Sr, $3d^6 4s^1$ for Mn and $2s^2 2p^4$ for O atoms, respectively. In performing energy minimization and subsequent electronic properties calculations, the plane-wave cutoff energy was chosen as 400 eV, and the Brillouin zone was sampled by using $5 \times 5 \times 3$ Gamma centered Monkhorst-Pack k-points grid. The convergence criterion for energy and force was set to 10^{-5} eV per unit cell and 0.01 eV/Å, respectively.

Within the GGA + U formalism, the value of the on-site Coulombic repulsion parameter U depends upon which compound the transition metal is a constituent of. For example, $U = 3$ eV was employed in modeling the magnetic properties of $\text{La}_{0.625}\text{Sr}_{0.375}\text{MnO}_3$ under high pressure [22], whereas for LaMnO_3 the value of U was chosen to be 4 eV [23]. Previous studies based on first-principles calculations using GGA (LDA) + U approach for perovskites containing Mn provide no consensus on the appropriate value of U. The Hubbard parameter U can, in fact, be calculated by the linear response theory (LRT) proposed by Cococcioni and Gironcoli et al. [24], who have demonstrated the accuracy of this method by computing structural and electronic properties of various systems including transition metals, rare-earth correlated metals and transition metal monoxides. We have thus calculated the effective on-site Coulomb repulsion parameter U_{eff} for $\text{La}_{2/3}\text{Sr}_{1/3}\text{MnO}_3$ by using the LRT that is internally consistent with the chosen definition for the occupation matrix of the relevant localized orbitals [24,25]. According to the LRT, the effective interaction parameter U_{eff} associated to site I can be written as

$$U_{\text{eff}} = \left(\chi_0^{-1} - \chi^{-1} \right)_I, \quad (1)$$

where χ^{-1} and χ_0^{-1} are the interacting and noninteracting Kohn–Sham density response functions of the system, respectively. They can be calculated by $\partial n_I / \partial \alpha_I$ and $\partial n_I / \partial \alpha_I^{\text{KS}}$, respectively, where n_I is the atomic orbital occupation for the atom I , and α_I (α_I^{KS}) denote

the interacting (noninteracting) Kohn–Sham localized perturbation potential. Using this method, we have calculated the response function of Mn and the resulting plot of d orbital occupation versus α is shown in Fig. 2. By changing the rigid potential shifts α , we obtain the bare and self-consistent occupation regression response functions. The interacting χ^{-1} and the Kohn textminus Sham χ_0^{-1} inverse matrices are the slopes of bare and self-consistent regression response functions, respectively. The resulting value of the Hubbard parameter U for Mn atom calculated from eq. (1) is 5.9 eV. The reliability of this calculated value of U can be further exemplified by noting that it is close to the value employed in our previous first-principles calculations (U = 6.0 eV) which yielded electronic structure results consistent with the X-ray absorption spectroscopic data [26].

The relative stability of defective LSMO with various charge states is determined by the formation energy. The formation energy of an oxygen vacancy in LSMO can be calculated from the total energy of the supercell using the Zhang–Northrup formalism [27]. According to this standard formalism, the formation energy of an oxygen vacancy with a charge state q ($E_f(O_V, q)$) is dependent on atomic and electronic chemical potentials, and is given by

$$E_f(O_V, q) = E_T(O_V, q) - E_T^{\text{ideal}} + E(O) + \mu_O + q\mu_e \quad (2)$$

where $E_T(O_V, q)$ (E_T^{ideal}) is the total energy of the supercells with (without) oxygen vacancy and $E(O)$ denotes the energy of an oxygen atom taken to be equal to half of that of an oxygen molecule $E(O_2)$ [28]. The chemical potential of an oxygen atom is denoted by μ_O and we set $\mu_O = 0$ in this work, which corresponds to the typical experimental condition of extreme O-rich limit. μ_e is the chemical potential of electron, i.e. the Fermi level. Two energy corrections are generally needed to take into account the interactions between the charged defect and the compensating background as well as its periodic images. One is the correction of valence band maximum considering that its value is different for supercell with and without a defect, owing to the defect-induced distortion of the band structure near the band edges [29–31]. In this paper, we apply this correction to Fermi level μ_e , the value of which is referenced to the valence band maximum. We first assume the potentials in the pristine system to be similar to those in the defective system at a far enough distance from a defect. We determined the average potential of the most distant plane from the defect in the defect-containing supercell (P_{av}^{defect}) and the average potential of the

corresponding plane in the pristine system (P_{av}^{perfect}). The difference in the two averaged potentials can then be used to correct μ_e as follows

$$\mu_e' = \mu_e + P_{av}^{\text{defect}} - P_{av}^{\text{ideal}} \quad (3)$$

The second necessary correction term is known as the Makov–Payne (M–P) correction, $q^2\alpha/2\epsilon L$, where ϵ is the static dielectric constant, L is the linear dimension of the supercell, and α is the Madelung constant [32]. This term describes the electrostatic energy of the point charge array in a uniform background in the presence of a screening medium described by the static dielectric constant [33]. For simplicity, we employ the value of Madelung constant as 2.8373, which corresponds to a simple cubic lattice [33].

3. Results and discussions

3.1. Structural comparison between vacancy-containing and ideal LSMO systems

First, we have carried out geometry optimization on the three supercell configurations shown in Fig. 1 using the GGA + U formalism, followed by calculations of their total energies. The calculated energy difference δ_{a-b} between cases (a) and (b) in Fig. 1 is -0.19 eV, and the energy difference δ_{a-c} between cases (a) and (c) in Fig. 1 is -0.20 eV. Therefore, the structure shown in Fig. 1(a) with no Sr atoms present at the first-nearest neighbor sites of vacancy in the ab-plane, is the most stable among the three cases. We chose the ferromagnetic ordering as the base of our calculations for the defective system since measurements based on X-ray absorption spectra and X-ray magnetic circular dichroism experiments [14], together with a theoretical phase diagram put forth by Fanget al. [34], have shown that the LSMO with the current set of lattice parameters exhibits ferromagnetic ordering.

It is generally believed that the inclusion of a Hubbard-like contribution to the Mn d states yields prominent changes in the electronic and magnetic properties but exerts insignificant influence on the structural properties as compared to bare DFT approaches [35]. In order to assess the influence of Hubbard U on the resultant optimized structure, we have carried out geometry optimization on the aforementioned configuration using both the GGA + U and the GGA formalisms. The profiles of the corresponding relaxed supercells in the bc-plane as well as the profile of the ideal system as a reference are depicted in Fig. 3. It can be readily observed that all the MnO_6 octahedra show various degrees of rotation with respect to the c-axis and the ab-plane. More importantly, the GGA + U formalism results in a larger angle of rotation than the GGA formalism. For example, the maximum angle of rotation with respect to the c-axis is 8.9° and 11.5° for the GGA and the GGA + U method, respectively. The Mn–O–Mn bond angles get reduced, due to such rotation of the octahedra, to as low as 162.3° with the GGA method and 157.1° for the GGA + U method. The MnO_6 rotation in the ab-plane is 13.6° for GGA + U and 5.5° for GGA formalism, respectively, which are not shown in this Figure. It thus becomes apparent that the GGA + U approach leads to a stronger modification in structural parameters.

Various structural parameters characterizing the relaxed systems are listed in Table 1. We first focus on the local structure surrounding the oxygen vacancy. The oxygen vacancy has two Mn atoms as the first-nearest neighbors, four La atoms as the second-nearest neighbors, and eight O atoms as the third-nearest neighbors. Compared with the ideal system, the two Mn atoms in the vacancy system move closer to each other by about 0.14 \AA (0.11 \AA) with the GGA + U (GGA) method. Similarly, the third-nearest neighboring oxygen atoms exhibit a tendency of moving closer

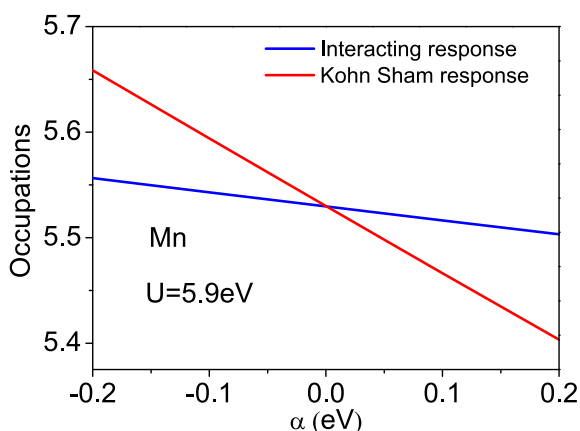


Fig. 2. Linear response of d orbital occupations to the change of potential shift α . The red and blue lines represent the Kohn–Sham and the noninteracting inverse density response functions, respectively. (For interpretation of the references to colour in this figure legend, the reader is referred to the web version of this article.)

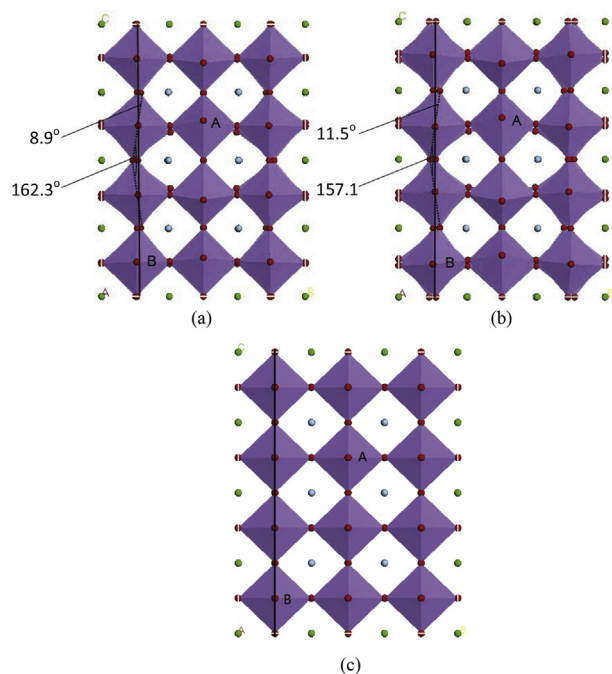


Fig. 3. The profile of the LSMO supercell in the bc-plane after structural relaxation with the (a) GGA formalism and (b) GGA + U formalism showing MnO₆ octahedral rotation. (c) the profile of ideal system as a reference. The upper and lower oblique lines point towards the maximum angle of rotation with respect to the c axis and the minimum Mn–O–Mn bond angle, respectively. The solid black line is added as visual aid to indicate the vertical direction. A and B label the first- and third-nearest neighbor MnO₆ octahedron of the oxygen vacancy, respectively.

toward the oxygen vacancy through a distance of nearly 0.56 Å (0.55 Å) with the GGA + U (GGA) method. However, the second-nearest neighboring La atoms move away from each other by nearly 0.21 Å and 0.18 Å for the GGA + U and the GGA method, respectively. The modifications in micro-environment of the oxygen vacancy are attributed to the rotation and deformation of MnO₆ octahedra and this modification is stronger for GGA + U than GGA results due to the more prominent octahedral modifications in the prior.

The oxygen-vacancy shortening of the Mn–Mn distance observed here is similar to the case of SrTiO₃, in which reduced Ti–Ti distance was found after the relaxation of vacancy-containing system using the HSE method [9]. In order to characterize the deformation of MnO₆ octahedra, we have listed in Table 1 the O–O

distances in the octahedron A and B (c.f. Fig. 3) which is the first-nearest neighbor and third-nearest neighbor of the oxygen vacancy in bc-plane, respectively. For the octahedron B, the O–O distances slightly increase along all the three axes as compared to the ideal system, except for its value along the c-axis given by the GGA method which remains nearly the same. For octahedron A, on the other hand, the O–O distances along the a- and c-axes increase while those along b-axis show slight decrease. In summary, the GGA + U approach leads to more prominent changes in interatomic distances.

3.2. Electronic structure changes induced by the inclusion of Hubbard U

The introduction of Hubbard parameter U in the GGA + U method yields structural changes in the defect-containing LSMO system as compared to the ideal system which are appreciably different than those obtained with the GGA method. Unsurprisingly, therefore, the electronic structure calculated by the two methods can also be expected to show important differences. In order to explore such differences, especially in the Mn 3d orbital electronic structure, we have plotted the density of states (DOS) of e_g and t_{2g} orbitals for Mn₁ (located in MnO₆ octahedron A) and Mn₃ (located at the first-nearest neighbor site of oxygen vacancy) in Fig. 4. The introduction of Hubbard U can be readily seen to give rise to a prominent change in the 3d orbitals electronic structures in both Mn₁ and Mn₃. The GGA + U DOS of e_g orbital does not exhibit any marked changes in the features as compared to the GGA DOS, especially in the low energy region. However, the DOS for the t_{2g} orbital by GGA + U method shows localized splitting of majority and minority spin peaks that lie farther apart from the Fermi level due to the strong Coulomb repulsion. For Mn₁, the exchange splitting of t_{2g} is about 2.84 eV with GGA, but 6.25 eV with GGA + U. Similarly, for Mn₃, its value increases from about 3.05 eV with GGA to about 5.94 eV with GGA + U. Therefore, the correlation between lattice and orbital has been magnified by including the on-site Coulombic repulsion parameter U for Mn 3d orbital, and this is just the reason why GGA + U leads to more prominent change of lattice structure which is different from the ideal system compared with GGA.

The calculated total DOS for LSMO is plotted in Fig. 5. The results obtained with the bare GGA method point to a behavior very close to, but not the true half-metallicity considering that the Fermi level exhibits a marginal shift into the conduction band of the minority spin states. The GGA + U derived results, on the other hand, clearly exhibit a gap in the minority spin states leading to a 100% spin

Table 1

Comparison of the structural parameters between the relaxed vacancy-containing supercell and the ideal supercell of the same size. The interatomic distances correspond two atoms diametrically opposite to the oxygen vacancy. NN denotes nearest neighbors. For the O–O distances, the values outside (inside) the bracket correspond to octahedron A (B).

Atom–atom distance (Å)	First NN (2 Mn)	Second NN (4 La)	Third NN (8 O)
Ideal	3.876	5.481	5.481
Vacancy (GGA)	3.764	5.660	4.932
Vacancy (GGA + U)	3.741	5.690	4.923
Mn–O–Mn bond angle (°)	a-axis	b-axis	c-axis
Ideal	180.0°	180.0°	180.0°
Vacancy (GGA)	163.3°	166.1°	162.3°
Vacancy (GGA + U)	157.3°	161.3°	157.1°
O–O distance in MnO ₆ octahedron A (B) (Å)	a-axis	b-axis	c-axis
Ideal	3.876	3.876	3.876
Vacancy (GGA)	3.965 (3.892)	3.827 (3.893)	3.888 (3.875)
Vacancy (GGA + U)	4.003 (3.893)	3.839 (3.903)	3.915 (3.883)
Maximum angle of rotation with respect to c-axis	8.9° (GGA)	11.5° (GGA + U)	

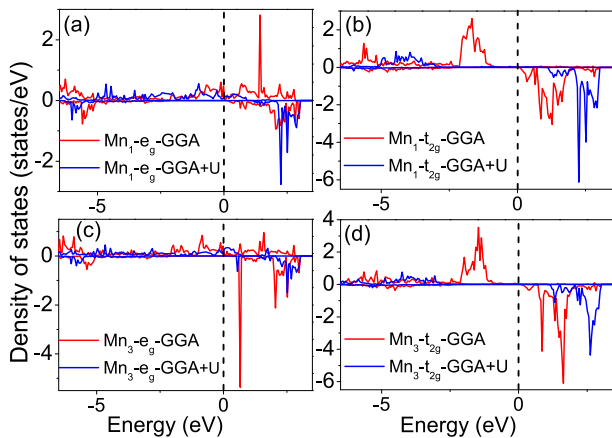


Fig. 4. The calculated 3d orbital DOS calculated with the GGA and GGA + U methods for Mn₁ (top panel) and Mn₃ (bottom panel) that are located in octahedron A and B, respectively. The e_g DOS is shown in (a) for Mn₁ and (c) for Mn₃. The t_{2g} DOS is shown in (b) for Mn₁ and (d) for Mn₃.

polarization of electrons at the Fermi level. Furthermore, calculations show that the total magnetic moment is 127.4 μ_B with the GGA method and 132.0 μ_B with the Hubbard-correction. The integer value obtained with the latter also points towards the true half-metallicity and is in agreement with the nearly 100% spin polarization observed experimentally in this system [36]. These results establish the accuracy and reliability of the results obtained with the GGA + U formalism for the defect-containing LSMO system, and we thus chose this method for the further detailed analysis presented in this paper.

3.3. Formation energy of the oxygen vacancy with different charge states in LSMO

We have calculated the formation energy of the oxygen vacancy in LSMO at different charge states $q = 1, -2, +1$ and $+2$ as well as the neutral state $q = 0$. As shown in Table 2, the system with $q = -2$ has the lowest vacancy-formation energy, indicating it to be the most stable among the different charge states. It can be noted that the formation energy of the defect in neutral state is relatively small at 0.04 eV. Such oxygen vacancy defect can thus easily form in

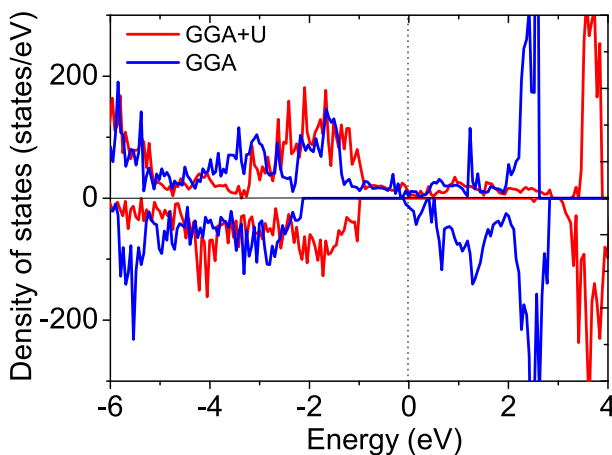


Fig. 5. The total DOS for the vacancy-containing LSMO supercells using GGA (blue curve) and GGA + U (red curve) formalisms. The vertical dotted line denotes the Fermi level. (For interpretation of the references to colour in this figure legend, the reader is referred to the web version of this article.)

Table 2

The calculated formation energy ($E_f(O_v, q)$ (eV)) of oxygen vacancy in charge states $q = -2, -1, +2, +1$ as well as neutral state $q = 0$.

Charge state	$q = -1$	$q = -2$	$q = 0$	$q = +1$	$q = +2$
$E_f(O_v, q)$ (eV)	-5.86	-11.34	0.04	6.35	13.07

LSMO under O-rich conditions. The negative formation energies for $q = -1$ and $q = -2$ imply that they can be spontaneously formed under O-rich conditions. The lowest formation energy is found for $q = -2$ indicating that the oxygen vacancy is a hole-type defect that tends to attract electrons. In order to examine this feature further, we have calculated the difference between the electron density in the system in $q = -2$ and in the neutral state $q = 0$. The resulting contour plot shown in Fig. 6 gives a clear picture of the electron density distribution of the net -2 charge. The oxygen vacancy at the center is surrounded by six red regions which represent the electron density concentration, indicating that it leads to a local negative charge concentration. This charge character of the oxygen vacancy may be expected to exert appreciable influence on the conductivity of this material.

3.4. Comparison of DOS in the oxygen-vacancy-containing and ideal LSMO

The calculated total DOS of LSMO in both the oxygen-vacancy-containing and the ideal system are depicted in Fig. 7. The results readily show that in both the ideal as well as defective systems, the characteristics of minority spin states correspond to those of an insulator or a semiconductor, whereas the majority spin states exhibit metallic characteristics. This indicates the half-metallic nature in this material resulting from the 100% spin polarization at the Fermi level. The half-metallicity of ideal LSMO system has been characterized in previous magnetotransport measurement [8,37] and also supported by theoretical studies [35]. Our results, importantly demonstrate that such half-metallic behavior is preserved in LSMO even in the presence of oxygen vacancy defects. In addition, the shape of the DOS in the vacancy-containing system is very similar to that in the ideal system.

For a deeper insight to the electronic structure, we have also calculated the partial DOS at different typical sites for Mn and O atoms. The octahedra A and B as shown in Fig. 3 correspond to the first-nearest neighbor and the third-nearest neighbor of the oxygen vacancy, respectively. As shown in Fig. 8, an O atom bonded to Mn atom in the ab-plane is denoted by O₁, whereas that bonded along the c-axis is denoted by O₂. In fact, there are two equivalent O₁

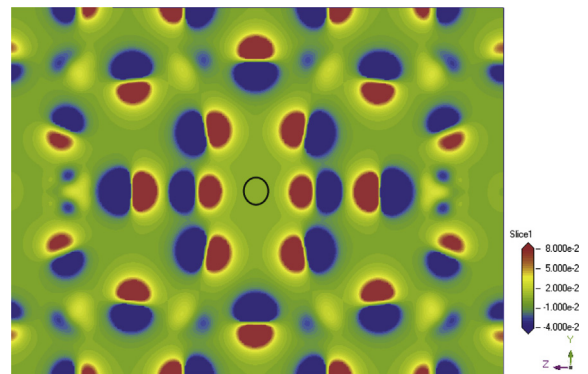


Fig. 6. Difference in the electron density between systems with the vacancy (black circle) in charge state $q = -2$ and $q = 0$. The electron density ranges from $-0.04 \text{ e}/\text{\AA}^3$ to $0.08 \text{ e}/\text{\AA}^3$.

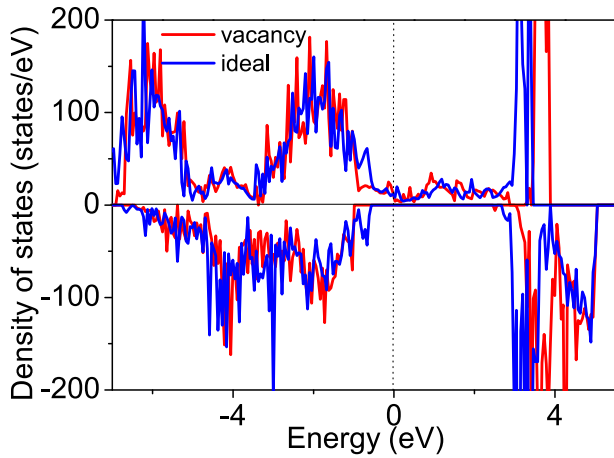


Fig. 7. The calculated total DOS of vacancy-containing and ideal LSMO. The vertical dotted line denotes the Fermi level.

atoms in *ab*-plane along the *x* and *y* directions, respectively. Fig. 9 presents the orbital DOS for Mn and O atoms of octahedron A for the ideal system and the vacancy-containing system. For the ideal as well as the defective system, the DOS corresponding to two e_g orbitals $3d_{3z^2-r^2}$ and $3d_{x^2-y^2}$, occupy the high energy regime whereas the t_{2g} DOS occupies the low energy regime, consistent with the general characteristics of electronic structure of LSMO [38]. Moreover, it can be inferred that O_1 and O_2 hybridize with Mn_1 3d orbital by the ligand orbital $2p_y$ and $2p_z$, respectively, as the finite DOS at the Fermi level appears only for these ligand orbitals. The Fermi level in the vacancy-containing system can also be noted to exhibit a shift toward the high energy regime as compared to that in the ideal system.

The calculated orbital DOS of Mn_2 and Mn_3 as well as the corresponding O_1 and O_2 are shown in Fig. 10 and Fig. 11, respectively. Similar to that noted for Mn_1 DOS, the Fermi level is found to shift to high energy regime for both of the partial DOS of all the atoms considered here. Such a Fermi level displacement may lead to an enhancement of the atomic magnetic moment of the three Mn atoms due to the lack of DOS for the minority spin states around the Fermi level, which will be discussed in further detail in the next subsection. In addition, one can note that the vacancy induced structural changes in MnO_6 octahedron result in a corresponding change in the ligand orbital DOS of oxygen atoms. In the results shown in Fig. 9 for octahedron A, as a result of Fermi level shift, the $2p_y$ DOS of O_1 and the $2p_z$ DOS of O_2 at the Fermi level show a slight enhancement and reduction, respectively, when compared with

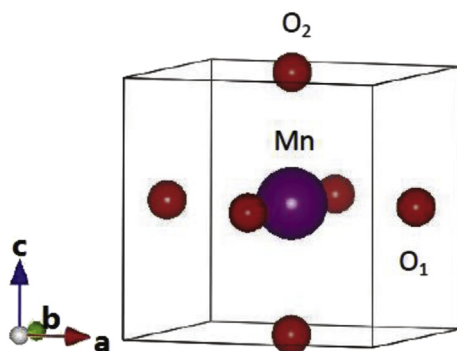


Fig. 8. Schematic of an MnO_6 octahedron denoting O_1 that bonds to the Mn atom in *ab*-plane and O_2 that bonds in *c* direction.

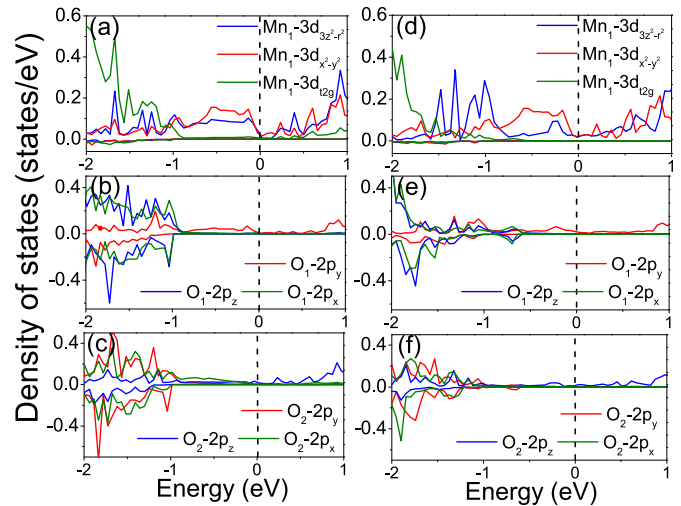


Fig. 9. The calculated orbital DOS for Mn, O_1 along *y* direction and O_2 atoms from the MnO_6 octahedron A for vacancy-containing (right panel) and ideal (left panel) LSMO. (a)–(c) correspond to Mn_1 3d orbitals, O_1 2p orbitals and O_2 2p orbitals of the ideal LSMO. (d)–(f) correspond similarly to vacancy-containing system.

the ideal system. This effect originates from the variations in the Mn–O distances discussed previously. The reduction of Mn–O distance along the *b*-axis leads to a stronger hybridization between the Mn 3d orbital and the O 2p orbital, leading to enhanced $2p_y$ DOS of O_1 . The elongation of Mn–O separation along the *c*-axis, on the other hand, results in a weaker hybridization between Mn 3d orbital and O 2p orbital. For octahedron B, as the Mn–O distance has increased for the *a*- and *c*-axis both, the $2p_x$ DOS of O_1 and $2p_z$ DOS of O_2 at the Fermi level are both suppressed, indicating weakening of the hybridization between Mn 3d orbital and O 2p orbital. The case of Mn_3 is special as it is located in an octahedron containing the oxygen vacancy, which leads to a missing Mn–O bond along the *c*-axis. Compared to the Mn–O bond length of 1.938 Å in both the *a*- and *c*-axes in the ideal system, Mn_3 in the defective system is separated from O atoms by 1.933 Å and 2.048 Å along the *a*- and *c*-axis (not shown in Table 1), respectively.

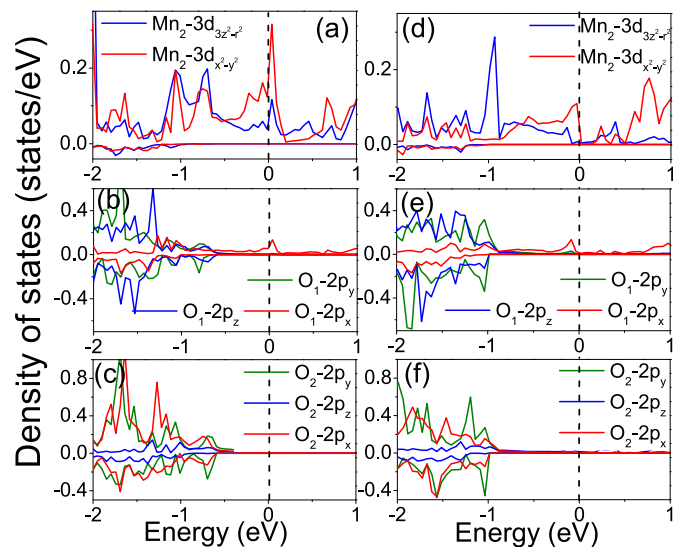


Fig. 10. The calculated orbital DOS for (a) $Mn_2 - 3d_{3z^2-r^2}$ and $Mn_2 - 3d_{x^2-y^2}$, (b) O_1 (*x*-direction) – 2p, and (c) $O_2 - 2p$ for ideal system; and (d) $Mn_2 - 3d_{3z^2-r^2}$ and $Mn_2 - 3d_{x^2-y^2}$, (e) O_1 (*x*-direction) – 2p, and (f) $O_2 - 2p$ for vacancy system.

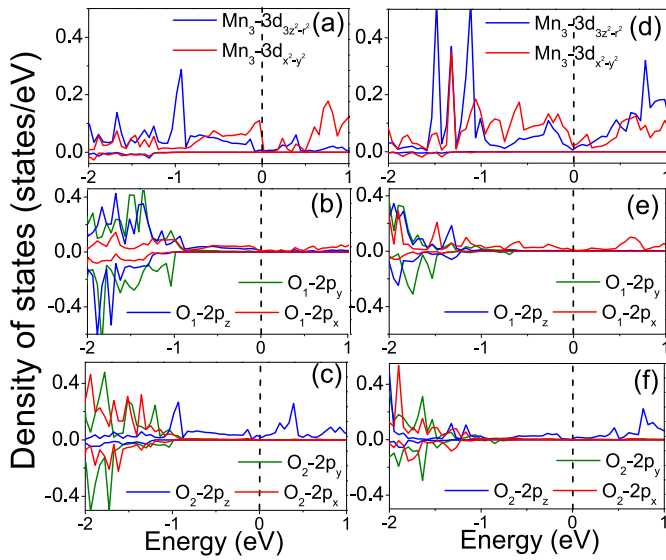


Fig. 11. The calculated orbital DOS for (a) $\text{Mn}_3-3d_{3z^2-r^2}$ and $\text{Mn}_3-3d_{x^2-y^2}$, (b) $\text{O}_1(x\text{-direction})-2p$, and (c) O_2-2p for ideal system; and (d) $\text{Mn}_3-3d_{3z^2-r^2}$ and $\text{Mn}_3-3d_{x^2-y^2}$, (e) $\text{O}_1(x\text{-direction})-2p$, and (f) O_2-2p for vacancy system.

Considering little deviation in the bond length along the a-axis and a slight increase along the c-axis, $2p_x$ DOS of O_1 at the Fermi level is nearly unmodified but the $2p_z$ DOS of O_2 at the Fermi level shows a decrease. This suppression of the $2p_z$ DOS of O_2 at the Fermi level may thus be attributed to the significant weakening of the hybridization between Mn 3d and O 2p orbitals due to one missing bond.

To explore detailed characteristics of Mn–O bonding, we investigate the bonding electron density in the bc-plane with the oxygen vacancy located at the center. The bonding electron density is defined as the difference between the total electron density in a solid and the superposition of neutral atomic electron densities at the same atomic sites. It thus represents the net electron redistribution as atoms are brought together to form the crystal. The positive and negative values in such plots represent gain and loss of electrons, respectively. The bonding electron density plotted in Fig. 12 shows an accumulation of electrons around the O atoms and loss around Mn atoms, pointing to the ionic properties of the Mn–O bonds. In addition, the distribution of the electron density at all the Mn and O sites exhibits in-planar rotation in accordance with the structural distortion of MnO_6 octahedra. It can be further found that the two Mn_3 atoms residing at the first-nearest neighbor sites of the oxygen vacancy exhibit different contour profiles than those in other sites. The electron density distribution recedes along the c-axis and extends along the b-axis. This remarkable change in the electron density distribution for Mn_3 atoms indicates that the Mn–O bonding weakens in the c-direction, but at the same time, gets strengthened in the ab-plane due to the introduction of the oxygen vacancy.

3.5. Comparison of magnetic properties of the vacancy-containing and ideal systems

The calculated magnetic moment, total valence electron number (VEN) and valence electron configuration of Mn_1 , Mn_2 and Mn_3 are presented in Table 3. The moments of La, Sr and O atoms have not been listed as their contribution to the total magnetism is negligible. The total magnetic moment of the $3 \times 3 \times 4$ supercell is an integer number, and is found to be $130 \mu_B$ for the ideal system and $132 \mu_B$ for the vacancy system. It points towards the half-metallicity

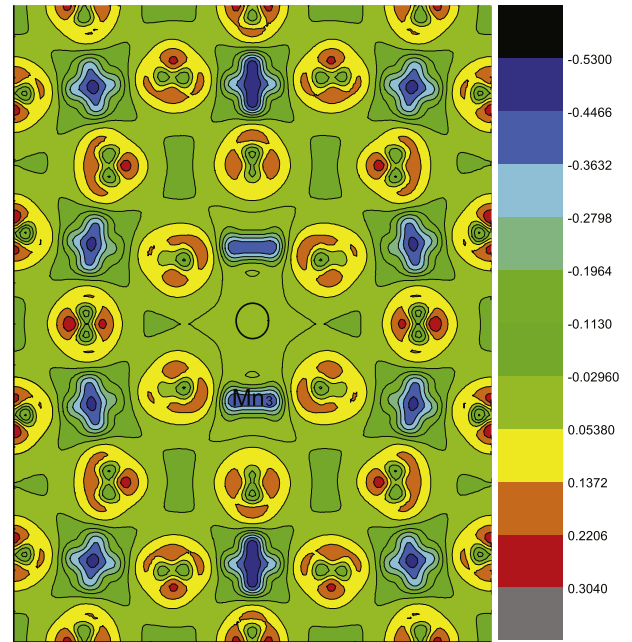


Fig. 12. The calculated bonding electron density in the bc-plane with the oxygen vacancy (black circle) is at the center. The site of Mn_3 which is the first-nearest neighbor of vacancy is also denoted. The maximum and minimum value plotted is $0.3040 \text{ e}/\text{\AA}^3$ and $-0.5300 \text{ e}/\text{\AA}^3$, respectively, with a contour step size of $0.0834 \text{ e}/\text{\AA}^3$.

of this material which is in agreement with the characteristics of the total DOS as discussed before. The enhancement in the total magnetic moment by introduction of the vacancy defect originates from the enhanced magnetic moments of Mn. In the perfect supercell, the magnetic moments of Mn_1 and Mn_3 , which are located in La–O surroundings are identical at $3.96 \mu_B$, while that of Mn_2 located in La–Sr–O surroundings has a relatively smaller value of $3.83 \mu_B$. These results are in agreement with the fact that the magnetic moment of Mn in LaMnO_3 is smaller than that in SrMnO_3 [35]. Furthermore, these calculated values are larger than those ($3.2 \sim 3.6 \mu_B$) reported in earlier theoretical studies, which adopt a value of the Hubbard U in a range from 0 to 3 [12,35], much smaller than that used in this work. It is known that the increase in U value leads to a corresponding increase in the magnetic moment [12]. More importantly, our results are in a superior agreement with the experimentally measured value of $\sim 3.7 \mu_B$ for LSMO grown on SrTiO_3 [35].

With the introduction of the vacancy defect, the magnetic moments of the three Mn atoms are enhanced by ($0.06 \mu_B$ for Mn_1 , $0.08 \mu_B$ for Mn_2 and $0.08 \mu_B$ for Mn_3). To understand the electronic origin of the modulation of magnetism, we have calculated the valence electron configuration using the Bader charge analysis [39,40] for both the defective and the ideal systems, the results of which are shown in Table 3. The total VENs are found to be identical

Table 3

The calculated atomic moment, total valence electron number (VEN) and valence electron configuration ('4s/3p/3d') corresponding to the Bader charge analysis of Mn_1 , Mn_2 and Mn_3 for defective and ideal systems. Total moments of $3 \times 3 \times 4$ supercell for vacancy and ideal systems are also listed for comparison.

Atom	Moment (μ_B)		VEN		4s/3p/3d	
	Ideal	Vacancy	Ideal	Vacancy	Ideal	Vacancy
Mn_1	3.96	4.02	5.06	5.06	0.26/0.47/4.33	0.26/0.39/4.41
Mn_2	3.83	3.91	5.02	5.02	0.31/0.45/4.26	0.27/0.40/4.35
Mn_3	3.96	4.04	5.10	5.17	0.25/0.44/4.41	0.28/0.41/4.49
Total	130	132				

between the systems with and without the defect, for Mn₁ (5.06) and Mn₂ (5.02). However, the VEN in Mn₃ of the defective system is greater than that in the ideal system by 0.07. This increase in the total VEN for vacancy-containing system can be directly related to the vacant oxygen site. Comparing the valence electron configuration of the defective system with the ideal system shows that the excess 0.08 electrons in the 3d orbital of Mn₁ come from the 3p orbital, whereas the excess of 0.09 electrons in the 3d orbital of Mn₂ come from both the 4s and 3p orbitals. Accordingly, such electron transfer leads to an enhancement of the magnetic moment since the five 3d orbitals tend to accommodate five electrons with parallel spins according to the Hund's Rule. Unlike Mn₁ and Mn₂, the increase of 0.08 3d electrons in Mn₃ is ascribed to the increased VEN rather than a transfer from the 3p orbital. Through a systematic analysis, we have thus resolved the correlations between the changes in the magnetic properties and the structure induced modification of bonding properties upon introduction of oxygen vacancy defects in LSMO.

4. Conclusions

In summary, we have elucidated the influence of oxygen vacancies on the structural, electronic and magnetic properties of La_{2/3}Sr_{1/3}MnO₃ by using the first-principles calculations with the Hubbard-corrected GGA + U formalism. The crucial parameter U representing the on-site Coulombic repulsion potential has been calculated to be 5.9 eV for Mn 3d orbital by employing the linear response theory. In the optimized geometry of the supercell of the vacancy-containing system, rotation as well as deformation of MnO₆ octahedra has been identified and such structural changes have been found to be more prominent with the GGA + U formalism than the bare GGA formalism. The oxygen vacancy alters its microenvironment such that its the first-nearest neighboring Mn atoms and the third-nearest neighboring O atoms move closer to each other, while the second-nearest neighboring La atoms move apart from each other when compared with the ideal system. Via calculation of the orbital DOS of Mn and O atoms occupying three typical sites in the supercell, we find that the distortions of MnO₆ octahedra exert a direct effect on the corresponding hybridization between the Mn 3d and the O 2p orbitals. While for Mn₁ located in MnO₆ A, the 3d orbital hybridization with 2p_y orbital of O₁ becomes stronger due to the reduced Mn–O bond length, that with the 2p_z orbital of O₂ weakens in accordance with the higher Mn–O separation. For Mn₂ located in MnO₆ B, the 3d orbital hybridization with both the 2p_x orbital of O₁ and the 2p_z orbital of O₂ weakens owing to Mn–O elongation along the a- and c-axes. The Mn atom (Mn₃) located at the first-nearest neighboring site of the defect also shows weakened hybridization between the Mn 3d and the 2p_z of O₂ orbitals.

It is further revealed that the magnetic moments of Mn₁, Mn₂ and Mn₃ show significant enhancement upon the introduction of the vacancy defect which originates in the increased number of valence electrons in the 3d orbitals as compared to those in the ideal system. Mn₁ and Mn₂ show a charge transfer from 4s and 3p to 3d while conserving the total number of valence electrons. On the other hand, Mn₃ also shows an increased total number of valence electron number owing to the loss of one bond with oxygen. Finally, calculations of the formation energy of an oxygen vacancy with different charge states, reveal rather small values suggestive of easy formation of the defective system under O-rich conditions. In addition, the oxygen vacancy in state q = –1 and q = –2 can be spontaneously formed owing to the negative formation energies. The lower formation energy of q = –2 compared with q = –1 indicates that the vacancy has the attributes of a hole-

type defect showing a tendency to form a negative charge center. Our work thus sheds light on the strong influence exerted by oxygen vacancies on the structural properties of LSMO, which in turn govern its electronic and magnetic properties.

Acknowledgments

This work is supported by the Singapore National Research Foundation through the Competitive Research Programme (CRP) under Project No. NRF-CRP5-2009-04.

References

- [1] R. von Helmolt, et al., *Phys. Rev. Lett.* 71 (1993) 2331.
- [2] S. Jin, T. Tiefel, M. McCormack, R. Fastnacht, R. Ramesh, L. Chen, *Science* 264 (1994) 413.
- [3] Y. Tokura, A. Urushibara, Y. Moritomo, T. Arima, A. Asamitsu, G. Kido, N. Furukawa, *J. Phys. Soc. Jpn.* 63 (1994) 3931.
- [4] A. Urushibara, Y. Moritomo, T. Arima, A. Asamitsu, G. Kido, Y. Tokura, *Phys. Rev. B* 51 (1995) 14103.
- [5] L.E. Hueso, J.M. Pruneda, V. Ferrari, G. Burnell, J.P. Valdés-Herrera, B.D. Simons, P.B. Littlewood, E. Artacho, A. Fert, N.D. Mathur, *Nat. (Lond.)* 445 (2007) 410.
- [6] R.K. Zheng, Y. Wang, H.L.W. Chan, C.L. Choy, H.S. Luo, *Phys. Rev. B* 75 (2007) 212102.
- [7] A.I. Buzdin, *Rev. Mod. Phys.* 77 (2005) 935.
- [8] M. Bowen, M. Bibes, A. Barth élémé, J.-P. Contour, A. Anane, Y. Lemaître, A. Fert, *Appl. Phys. Lett.* 82 (2003) 233.
- [9] C. Mitra, C. Lin, J. Robertson, Alexander A. Demkov, *Phys. Rev. B* 86 (2012) 155105.
- [10] W. Siemons, G. Koster, H. Yamamoto, W.A. Harrison, G. Lucovsky, T.H. Geballe, D.H.A. Blank, M.R. Beasley, *Phys. Rev. Lett.* 98 (2007) 196802.
- [11] X. Xiang, L. Qiao, H.Y. Xiao, F. Gao, X.T. Zu, S. Li, W.L. Zhou, *Sci. Rep.* 4 (2014) 5477.
- [12] S. Picozzi, C. Ma, Z. Yang, R. Bertacco, M. Cantoni, A. Cattoni, D. Petti, S. Brivio, F. Ciccacci, *Phys. Rev. B* 75 (2007) 094418.
- [13] F. Tsui, M.C. Smoak, T.K. Nath, C.B. Eom, *Appl. Phys. Lett.* 76 (2000) 2421.
- [14] Y. Takamura, R.V. Chopdekar, E. Arenholz, Y. Suzuki, *Appl. Phys. Lett.* 92 (2008) 162504.
- [15] M. Imada, A. Fujimori, Y. Tokura, *Rev. Mod. Phys.* 70 (1998) 1039.
- [16] M.B. Salamon, M. Jaime, *Rev. Mod. Phys.* 73 (2001) 583.
- [17] G. Kresse, J. Furthmüller, *Phys. Rev. B* 54 (1996) 11169.
- [18] G. Kresse, D. Joubert, *Phys. Rev. B* 59 (1999) 1758.
- [19] P.E. Blöchl, *Phys. Rev. B* 50 (1994) 17953.
- [20] J.P. Perdew, K. Burke, M. Ernzerhof, *Phys. Rev. Lett.* 77 (1996) 3865.
- [21] J.P. Perdew, J.A. Chevary, S.H. Vosko, A. Jackson, M.R. Pederson, C. Fiolhais, *Phys. Rev. B* 46 (1992) 6671.
- [22] Giuseppe Colizzi, Alessio Filippetti, Vincenzo Fiorentini, *Phys. Rev. B* 76 (2007) 064428.
- [23] C. Franchini, R. Kováčik, M. Marsman, S. Sathyanarayana Murthy, J. He, C. Ederer, G. Kresse, *J. Phys. Condens. Matter* 24 (2012) 235602.
- [24] Matteo Cococcioni, Stefano de Gironcoli, *Phys. Rev. B* 71 (2005) 035105.
- [25] Junjie He, Na Jiao, Chunxiao Zhang, Huaping Xiao, Xiaoshuang Chen, *J. Lichong Sun, Phys. Chem. C* 118 (2014) 8899.
- [26] Baomin Wang, Lu You, Peng Ren, Xinmao Yin, Yuan Peng, Bin Xia, Lan Wang, Xiaojiang Yu, Sock Mui Poh, Ping Yang, Guoliang Yuan, Lang Chen, Andriwo Rusydi, Junling Wang, *Nat. Commun.* 4 (2013) 2778.
- [27] S.B. Zhang, J.E. Northrup, *Phys. Rev. Lett.* 67 (1991) 2339.
- [28] A. Janotti, J.B. Varley, P. Rinke, N. Umezawa, G. Kresse, C.G. Van de Walle, *Phys. Rev. B* 81 (2010) 085212.
- [29] L. Xue, D.H. Tang, X.D. Qu, L.Z. Sun, Wei Lu, J.X. Zhong, *J. Appl. Phys.* 110 (2011) 053704.
- [30] L. Xue, P. Zhou, C.X. Zhang, L.Z. Sun, Jianxin Zhong, *J. Phys. Chem. Solids* 74 (2013) 1086.
- [31] D.B. Laks, C.G. Van deWalle, G.F. Blöchl, S.T. Pantelides, *Phys. Rev. B* 45 (1992) 10965.
- [32] G. Makov, M.C. Payne, *Phys. Rev. B* 51 (1995) 4014.
- [33] J. Lento, J.-L. Mozos, R.M. Nieminen, *J. Phys. Condens. Matter* 14 (2002) 2637.
- [34] Z. Fang, I.V. Solovyev, K. Terakura, *Phys. Rev. Lett.* 84 (2000) 3169.
- [35] Chunlan Ma, Zhongqin Yang, J. Silvia Picozzi, *Phys. Condens. Matter* 18 (2006) 7717.
- [36] J.L. Maurice, F. Pailloux, A. Barthelemy, O. Durand, D. Imhoff, R. Lyonnet, A. Rocher, J.P. Contour, *Philos. Mag.* 83 (2003) 3201.
- [37] M. Bowen, A. Barthélémy, M. Bibes, E. Jacquet, J.-P. Contour, A. Fert, F. Ciccacci, L. Duò, R. Bertacco, *Phys. Rev. Lett.* 95 (2005) 137203.
- [38] D.J. Singh, W.E. Pickett, *J. Appl. Phys.* 83 (1998) 7354.
- [39] Jie Li, M.L. Hu, Zhizhou Yu, J.X. Zhong, L.Z. Sun, *Chem. Phys. Lett.* 532 (2012) 40.
- [40] G.C. Zhou, L.Z. Sun, X.L. Zhong, Xiaoshuang Chen, Lu Wei, J.B. Wang, *Phys. Lett. A* 368 (2007) 112.